Class. Quantum Grav. **26** (2009) 085009 (30pp) doi:10.1088/0264-9381/26/8/085009

Gravitational wave burst search in the Virgo C7 data

F Acernese[1ac], M Alshourbagy[2ab], F Antonucci[3a], S Aoudia[4], K G Arun[5], P Astone[3a], G Ballardin[6], F Barone[1ac], L Barsotti[2ab], M Barsuglia[7], Th. S Bauer[8a], S Bigotta[2ab], S Birindelli[4], M-A Bizouard[5], C Boccara[9], F Bondu[4], L Bonelli[2ab], L Bosi[10a], S Braccini[2a], C Bradaschia[2a], A Brillet[4], V Brisson[5], H J Bulten[8ab], D Buskulic[11], G Cagnoli[12a], E Calloni[1ab], E Campagna[12ac], B Canuel[6], F Carbognani[6], L Carbone[10a], F Cavalier[5], R Cavalieri[6], G Cella[2a], E Cesarini[12ab], E Chassande-Mottin[7], S Chatterji[3a], N Christensen[6], A-C Clapson[5], F Cleva[4], E Coccia[13ab], M Colombini[3b], C Corda[2ab], A Corsi[3a], F Cottone[10ab], J-P Coulon[4], E Cuoco[6], S D'Antonio[13a], A Dari[10ab], V Dattilo[6], M Davier[5], R De Rosa[1ab], M Del Prete[2ac], L Di Fiore[1a], A Di Lieto[2ab], M Di Paolo Emilio[13ad], A Di Virgilio[2a], V Fafone[13ab], I Ferrante[2ab], F Fidecaro[2ab], I Fiori[6], R Flaminio[14], J-D Fournier[4], S Frasca[3ab], F Frasconi[2a], L Gammaitoni[10ab], F Garufi[1ab], E Genin[6], A Gennai[2a], A Giazotto[2a,6], M Granata[7], V Granata[11], C Greverie[4], G Guidi[12ac], H Heitmann[4], P Hello[5], S Hild[15], D Huet[6], P La Penna[6], M Laval[4], N Leroy[5], N Letendre[11], M Lorenzini[12a], V Loriette[9], G Losurdo[12a], J-M Mackowski[14], E Majorana[3a], N Man[4], M Mantovani[6], F Marchesoni[10a], F Marion[11], J Marque[6], F Martelli[12ac], A Masserot[11], F Menzinger[6], C Michel[14], L Milano[1ab], Y Minenkov[13a], S Mitra[4], J Moreau[9], N Morgado[14], M Mohan[6], A Morgia[13ab], S Mosca[1ab], B Mours[11], I Neri[10ab], F Nocera[6], G Pagliaroli[13ad], C Palomba[3a], F Paoletti[2a,6], S Pardi[1ab], A Pasqualetti[6], R Passaquieti[2ab], D Passuello[2a], G Persichetti[1ab], F Piergiovanni[12ac], L Pinard[14], R Poggiani[2ab], M Punturo[10a], P Puppo[3a], O Rabaste[7], P Rapagnani[3ab], T Regimbau[4], F Ricci[3ab], A Rocchi[13a], L Rolland[11], R Romano[1ac], P Ruggi[6], B Sassolas[14], D Sentenac[6], B L Swinkels[6], R Terenzi[13ac], A Toncelli[2ab], M Tonelli[2ab], E Tournefier[11], F Travasso[10ab], G Vajente[2ab], J F J van den Brand[8ab], S van der Putten[8a], D Verkindt[11], F Vetrano[12ac], A Viceré[12ac], J-Y Vinet[4], H Vocca[10a], M Was[5] and M Yvert[11]

[1] INFN, sezione di Napoli[a]; Università di Napoli 'Federico II'[b], Complesso Universitario di Monte S. Angelo, I-80126 Napoli; Università di Salerno[c], Fisciano, I-84084 Salerno, Italy
[2] INFN, Sezione di Pisa[a]; Università di Pisa[b]; I-56127 Pisa; Università di Siena[c], I-53100 Siena, Italy
[3] INFN, Sezione di Roma[a]; Università 'La Sapienza'[b], I-00185 Roma, Italy
[4] Département Artemis, Observatoire de la Côte d'Azur, CNRS, F-06304 Nice, France
[5] LAL, Université Paris-Sud, IN2P3/CNRS, F-91898 Orsay, France
[6] European Gravitational Observatory (EGO), I-56021 Cascina (Pi), Italy
[7] AstroParticule et Cosmologie (APC), CNRS: UMR7164-IN2P3-Observatoire de Paris-Université Denis Diderot-Paris VII-CEA : DSM/IRFU, France
[8] National institute for subatomic physics[a], NL-1009 DB; Vrije Universiteit[b], NL-1081 HV, Amsterdam, The Netherlands
[9] ESPCI, CNRS, F-75005 Paris, France
[10] INFN, Sezione di Perugia[a]; Università di Perugia[b], I-6123 Perugia, Italy

0264-9381/09/085009+30$30.00

[11] Laboratoire d'Annecy-le-Vieux de Physique des Particules (LAPP), IN2P3/CNRS, Université de Savoie, F-74941 Annecy-le-Vieux, France
[12] INFN, Sezione di Firenze[a], I-50019 Sesto Fiorentino; Università degli Studi di Firenze[b], I-50121 Firenze; Università degli Studi di Urbino 'Carlo Bo'[c], I-61029 Urbino, Italy
[13] INFN, Sezione di Roma Tor Vergata[a]; Università di Roma Tor Vergata[b], Istituto di Fisica dello Spazio Interplanetario (IFSI) INAF[c], I-00133 Roma; Università dell'Aquila[d], I-67100 L'Aquila, Italy
[14] Laboratoire des Matériaux Avancés LMA, IN2P3/CNRS, F-69622 Villeurbanne, Lyon, France
[15] School of Physics & Astronomy University of Birmingham B15 2TT, UK

Received 20 January 2009, in final form 9 March 2009
Published 1 April 2009
Online at stacks.iop.org/CQG/26/085009

Abstract
A search for gravitational wave burst events has been performed with the Virgo C7 commissioning run data that have been acquired in September 2005 over 5 days. It focused on unmodeled short duration signals in the frequency range 150 Hz to 2 kHz. A search aimed at detecting the GW emission from the merger and ring-down phases of binary black hole coalescences was also carried out. An extensive understanding of the data was required to be able to handle a burst search using the output of only one detector. A 90% confidence level upper limit on the number of expected events given the Virgo C7 sensitivity curve has been derived as a function of the signal strength, for unmodeled gravitational wave searches. The sensitivity of the analysis presented is, in terms of the root sum square strain amplitude, $h_{rss} \simeq 10^{-20}$ Hz$^{-1/2}$. This can be interpreted in terms of a frequentist upper limit on the rate $\mathcal{R}_{90\%}$ of detectable gravitational wave bursts at the level of 1.1 events per day at a 90% confidence level. From the binary black hole search, we obtained the distance reach at 50% and 90% efficiency as a function of the total mass of the final black hole. The maximal detection distance for non-spinning high and equal mass black hole binary system obtained by this analysis in C7 data is $\simeq 2.9 \pm 0.1$ Mpc for a detection efficiency of 50% for a binary of total mass 80 $M_{\odot}$.

PACS numbers: 04.80.Nn, 04.30.Tv, 95.30.Sf, 95.85.Sz

(Some figures in this article are in colour only in the electronic version)

1. Introduction

Virgo [1] is a 3 km long arm power-recycled Michelson interferometer located near Pisa, Italy, whose goal is to detect gravitational waves (GW) emitted by astrophysical sources extending out past the Virgo cluster. The commissioning of the detector started in 2003 and regular data taking campaigns have been organized after each important milestone. The last commissioning run (C7) took place in September 2005 and lasted for 5 days. The best achieved sensitivity was $h \simeq 7 \times 10^{-22}$ Hz$^{-1/2}$ at 300 Hz. The Virgo design sensitivity at this frequency is expected to be better by an order of magnitude assuming that 10 W enters into the interferometer. However, during the C7 run, Virgo was running with a reduced light power, 0.7 W, because the backscattering in the mode-cleaner cavity of the light reflected by the recycling mirror

prevented the control of the interferometer at full power. Despite the reduced sensitivity, several GW searches have been carried out using this data set in order to set up and tune the pipelines developed in Virgo: the search of the coalescence of neutron stars [2], the search of continuous wave sources [3], a joint Virgo, AURIGA, EXPLORER and NAUTILUS GW search [4], a targeted GW burst search associated with the long GRB 050915a [5], and the search of GW burst signals that is reported in this paper.

The category of gravitational wave bursts includes all possible signals whose duration is short, less than a few hundreds of milliseconds. Many violent astrophysical phenomena will be accompanied by an emission of GW burst. If these events happen sufficiently close by, the ground based gravitational detectors will be able to observe these short duration GW bursts. There are many candidate GW burst sources. These include massive star core collapse [6–11], the merging phase of coalescing compact binary systems forming a single black hole (BH) [12–15], BH ring down [16], astrophysical engines that generate gamma-ray bursts (GRB) [17], neutron star oscillation modes and instabilities [18] or cosmic string cusps and kinks [19]. Some of these sources are well modeled, but not all, and as such a burst pipeline is built by making very few assumptions about the nature of these waveforms. The theoretical event rates for many of these sources are quite uncertain.

Binary black hole (BBH) mergers are an interesting source for GW burst searches. The typical event rate for these sources is 1 Myr^{-1} per galaxy [20, 21] and is still highly uncertain given the lack of direct observational evidence for the existence of BBH systems, unlike the double neutron star systems. Though these sources are routinely searched for by the inspiral phase prior to merger using matched filtering techniques, an independent search focusing on the merger and ring-down GW emission, which is dominant for high mass binaries [12], may bring additional confidence[16]. A search of this type was first attempted with the LIGO S2 data [22]; this used the then-available numerical relativity waveforms from the Lazarus project as a model of BBH mergers. However the estimates obtained were projected as order of magnitude estimates due to the nonrobusteness of the waveforms used. Though the burst searches do not have as large of a distance reach as an inspiral search, it will be interesting to understand the implications of a BH binary search from a burst perspective, especially because a burst search is sensitive to the merger and ring-down phase of a BBH coalescence. Among the three phases of inspiral, merger and ring down, for the BBH most of the energy is released in the highly relativistic phase of merger, that is difficult to model by analytic approximation methods. But recently numerical relativity simulations have made significant advances in generating the waveforms for all the three phases of the binary evolution (see [23] and references therein).

In this paper, we report on an all-sky burst search for unmodeled waveforms and BBH mergers without using any prior information on the expected waveform. This concerns all short duration ($\ll$1 s) signals having energy in the best sensitivity frequency band of the C7 data, 150–2000 Hz. This search has been performed using the data of only one interferometer which does not allow one to perform timing coincidence to eliminate spurious events in one of the detectors, as was done in the burst searches performed using the LIGO detectors [22, 24, 25] and the bar detectors [26]. However, a similar one-detector burst search has already been carried out with the data from the TAMA detector [27]. The C7 run data has been used for extensive analysis of the Virgo noise; this is a fundamental step in the path toward performing a GW burst search with only one detector. Indeed, numerous sources of noise generate, in the interferometer's GW strain amplitude channel, transient events which mimic GW burst events; environmental noise, such as acoustic noise, has been found at the origin of many of them.

[16] Template based searches for binary black hole sources using different waveforms which capture the different phases, including merger and ring down, are now applied to analyze the LIGO and Virgo data.

Non-stationary data can also generate an excess of short duration events. Such phenomena have been found, examined, and understood in the C7 data. These studies allowed us to define the pre-processing and post-processing steps needed in order to optimize the performance of the GW burst pipeline used in this analysis.

The outline of this paper is as follows. In section 2 we describe the main features of the Virgo detector, emphasizing the operating characteristics during the C7 run that played a role in understanding the quality of the data. In section 2.2 we describe how we select the data periods that have been used for this analysis. The burst pipeline used in this analysis is described in section 3. In section 3.4 the main results on the C7 data characterization needed in order to understand and to suppress the sources of glitches are summarized; this includes the veto strategy used against identified sources of noise. Section 4 gives the results of the search in the C7 data. Section 5 explains how the analysis sensitivity has been estimated considering different types of possible GW burst waveforms. We especially considered in this paper BBH merger and ring-down numerical waveforms [28]. Section 6 gives the upper limits obtained at 90% of confidence level on the number of events as a function of the signal strain amplitude. We finally conclude this paper with an astrophysical interpretation of the present GW burst search.

2. Virgo during the commissioning run C7

2.1. Detector status

The Virgo detector [29] is a power-recycled Michelson interferometer with 3 km long arms that each contain a Fabry–Perot cavity. All mirrors are suspended from the so-called superattenuator [30], whose goal is to reduce drastically above 10 Hz the seismic noise transferred to the instrument. A 20 W Nd:YAG laser is used to illuminate the interferometer. The laser light is modulated in phase at the frequencies $\simeq$22 and 6 MHz; this technique permits the GW strain to be detected at the modulation frequency where the laser power fluctuation is much smaller than in the interferometer bandwidth. The beam is spatially filtered with a 144 m long triangular input mode-cleaner cavity before being injected into the main interferometer. The laser frequency is pre-stabilized in order to acquire the control of the different optical cavities, but to reach the extreme sensitivity targeted by Virgo an enhanced control of the laser frequency noise is required; it has to be reduced by several orders of magnitude. This is the role of the so-called *second stage frequency stabilization* which is engaged during the cavities' lock acquisition [31]. The beam entering the interferometer is divided by the beam splitter (BS) into two beams that are injected into the 3 km long arm cavities. Apart from the mirrors' losses, all light fed-in by the injection system subsequently returns to it. The power-recycling (PR) mirror, with a reflectivity of 92%, reflects the out-going light back to the main interferometer. Together with the Michelson interferometer the power-recycling mirror forms a Fabry–Perot-like cavity in which the light power is resonantly enhanced, thereby improving the shot noise limit. The Michelson interferometer is held on the dark fringe, and the GW strain signal is expected in the beam at the dark port, which leaves the vacuum via the so-called detection bench. The detection bench is a suspended table accommodating several optical components. The beam coming from the BS passes through an output mode cleaner, a 3.6 cm long rigid cavity. The main output beam is detected by a pair of InGaAs photodiodes. Useful signals are obtained by detecting the light in the transmission of the arm cavities and in reflection of the power-recycling cavity (B2 photodiode). The GW signal that results from a detuning of the carrier resonance in the arms is extracted from the dark port channel, demodulated and then sampled at 20 kHz. This signal is digitized and filtered.

The control of the interferometer consists in maintaining the laser light resonant in the optical cavities and the output port tuned on the dark fringe, defining its working point. More precisely, the carrier must be resonant in all cavities while the sidebands must be resonant in the central cavity but anti-resonant in the arms. Despite the good seismic noise attenuation provided by the superattenuator, feedback controls are mandatory in order to keep the interferometer locked on the right working point. In addition to the control of the longitudinal degrees of freedom of the cavities, the mirrors must be kept aligned with respect to each other. This is the so-called auto-alignment control (AA). If uncontrolled, the angular degrees of freedom of the suspended optics distort the cavity eigen modes. This causes power modulation of the light fields; furthermore, long term drifts will make the longitudinal control impossible after a certain amount of time, and misalignments increase the coupling of other noise sources into the dark port. This has been a major problem in the C7 data analysis (see section 3.4). In actuality, during C7 not all of the mirrors were under AA control; the arm input mirrors and the injection bench were only controlled locally.

To convert the signal received on the dark port into a measure of GW strain one needs to calibrate the residual arm-length difference; this includes at low frequencies the effect of the control loop keeping the cavities in resonance. The loop correction signals are subtracted from the dark port signal that is then converted into a strain via knowledge of the optical gain of the feedback control loops. This gain may vary depending, for instance, on the alignment drifts of the optical elements. To monitor the variation, some sinusoidal signals (four between 100 and 110 Hz, and four between 350 and 360 Hz) are applied on the end-arm mirrors and the amplitude of the lines are measured. Another important aspect of the GW strain reconstruction is the good knowledge of the transfer function of the actuator chain which is used to control the mirrors. Actually, during the C7 run, the calibration procedure was not as accurate as it is now. For instance, the frequency dependence of the digital to analog converter transfer function was not taken into account in the reconstruction of the GW strain amplitude channel $h(t)$. This yielded a systematic error on $h(t)$ which has been estimated to be 40% [32].

Moreover, during C7 Virgo was running with a 700 mW laser beam entering the interferometer in order to avoid instabilities due to the backscattering of light into the mode-cleaner cavity reflected by the recycling mirror. The problem has since been fixed during a shutdown carried out just after the C7 run. This reduced power light limited the sensitivity at high frequencies. Figure 1 displays and compares the progress achieved on the sensitivity curve since the beginning of the Virgo commissioning. At high frequencies ($>$300 Hz), the sensitivity was limited by the shot noise and the laser frequency noise. At low frequencies ($<$100 Hz) the longitudinal and angular controls of the mirrors are the main limitation; the electronic noise of the actuator and/or the sensor introduced by the control loops induce a displacement of the mirror which is well above the fundamental noise floor.

2.2. C7 data set

After the lock acquisition is completed, the interferometer state is set to *science mode*. The science mode duty cycle maintained by Virgo during C7 was 66%. The data was split into 53 data blocks, or segments, spanning over the 5 days. A minimal duration of 10 min has been required for a segment. In order to define the start and end time of the data segments of good quality for the search for burst GW events we considered all the known instrumental effects that influence and spoil the output of the burst pipeline. For example, the last 10 s of each segment has been removed because many signals, including the GW strain channel, start oscillating and thereby cause the loss of lock. Another problem concerns the excitation of some thermal resonances of the last stage of the suspension (violin modes) when attempting

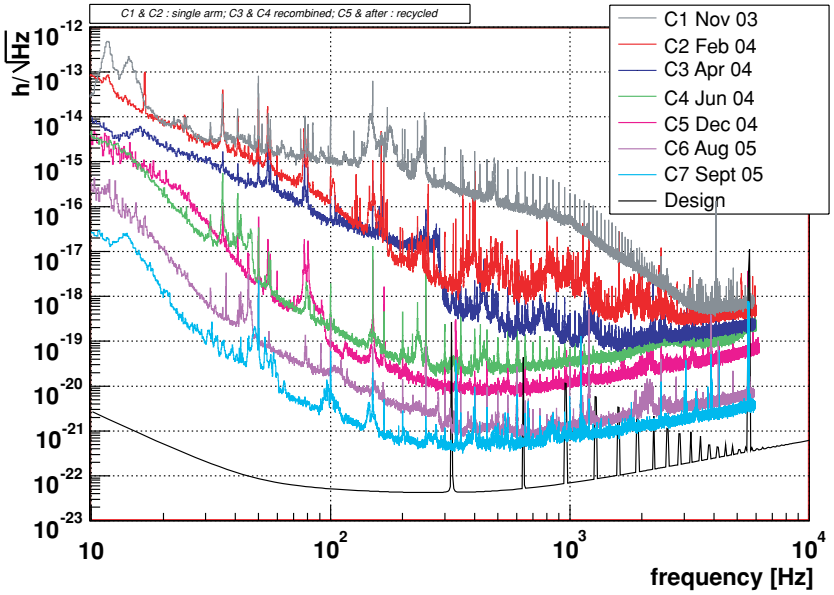

Figure 1. Sensitivity curves obtained between 2003 and 2005 during the commissioning of the Virgo detector before the 2005 shutdown. The black curve is the Virgo nominal sensitivity curve which has been computed assuming a 10 W laser.

to lock the interferometer. The decay time of these resonances has been determined, and for each segment we suppressed the beginning until the amplitude of the resonance having the longest decay time has been decreased by 90%. The reduction of the size of the data segments (hereafter called *science segments*) due to these data quality criteria amounts to 8%. In addition, some signals have been artificially injected into the GW strain channel during C7 by applying a force on the input mirror of one of the interferometer arm's Fabry–Perot cavity. These are the so-called hardware injections. The hardware injection signals are used in this analysis to test that the vetoes against external sources of noise that were implemented do not suppress any potentially real GW events (see section 3.4.4). The hardware injection periods were not considered for the GW burst search. Taking into account the application of the data quality criteria and the hardware injection periods, the duty cycle is finally reduced from 66% to 55%. This corresponds to a total duration of 2.51 days.

3. Description of the burst search pipeline

3.1. Overview

The GW burst pipeline that has been used in this search is composed of several parts that allow us to select and analyze all segments of Virgo data and eliminate, as much as possible, the artifacts in the detector output that could mimic a GW event. The core of the pipeline is the GW detection statistic, described in section 3.3, that is applied on pre-selected segments of data of good quality. This results in lists of triggers. As we are dealing with non-Gaussian and non-stationary data, many of these triggers are due to instrumental effects. The next step consists of identifying all the sources of noise disturbances that pollute the detector output, and then define vetoes to be applied *a posteriori* on the trigger lists. This step in this pipeline

is playing an important role as we cannot suppress these artifacts by requesting coincidence with another detector. We provide details on how the vetoes have been defined and which sources of noise they help in suppressing.

3.2. Data selection

Instrumental problems and environmental conditions have been identified that temporarily affect the detector sensitivity for a GW burst search. In a pre-selection step, we discard the periods where the detector operation is not optimal. To do so, we have defined a list of data quality flags (DQ) that highlight the intervals of malfunctioning. Among the DQ flags, some pertain to the saturation of the photodiodes and/or actuator signals that are used to keep the interferometer locked to its operating point. The analog electronics of the control loop that maintains the laser frequency noise below the requirements was sometimes also saturating. That then induces incorrect control signals and consequently a misbehaving GW strain amplitude. An excess of events was found when the GW strain $h(t)$ reconstruction process was facing a problem, for instance when the calibration lines were buried in the noise. When this happens the $h(t)$ reconstruction program sets a DQ flag stored in the data stream. Sometimes during C7 a few frames or channels were missing due to some failure of the data acquisition system. That produces a hole in the continuous time series. The burst pipelines manage properly with the presence of holes in a segment, but to accurately compute the effective duty cycle we have defined a DQ flag pertaining to this issue. Finally, it has been found that when an aircraft is flying above the interferometer at a relatively low altitude acoustic and/or seismic noise couples into the dark fringe beam and induces a strong effect in $h(t)$ that is detected by the burst pipelines. The band limited RMS of some acoustic probes (located in the end arm buildings) were monitored to detect the airplanes. All these DQ segments have been combined into a single list, taking into account possible overlaps. The dead time induced by the application of these DQ flags on triggers list was only 0.8%, of the total duration which is acceptably low.

3.3. Event trigger generation: exponential Gaussian correlator

Different pipelines have been developed to search for GW bursts. Many of them [33–36] rely on a common principle i.e., the detection of clusters of excess energy in a time-frequency representation of the data. The pipeline we use in this analysis follows the same idea; we refer to it as the exponential Gaussian correlator (EGC) as it been described in [37], but here we give a short summary.

The time-frequency plane can be tiled using a lattice of sine Gaussian waveforms i.e.,

$$\Phi(t) = \exp\left(-\frac{1}{2}\left(\frac{t}{\tau_0}\right)^2\right) \mathrm{e}^{2\pi \mathrm{i} f_0 t}, \tag{1}$$

where the values of the central frequency f_0 and typical duration τ_0 can be chosen in such way as to optimize the coverage of the plane. The idea is to consider the above waveforms as typical burst transients and to search for them using a matched filtering technique. For this reason, we designate $\Phi(t)$ as a template waveform. The EGC computes the cross-correlation of the data with the templates, namely

$$C(t) = \frac{1}{N}\int_{-\infty}^{+\infty} \frac{\tilde{x}(f)\tilde{\Phi}^*(f)}{S(f)} \mathrm{e}^{2\pi \mathrm{i} f t}\, \mathrm{d}f, \tag{2}$$

where $\tilde{x}(f)$ and $\tilde{\Phi}(f)$ are the Fourier transforms of the data and template, and $S(f)$ is the two-sided power spectral density of the noise. N is the normalization factor of the templates defined as

$$N = \sqrt{\int_{-\infty}^{+\infty} \frac{|\Phi(f)|^2}{S(f)}\,\mathrm{d}f}, \tag{3}$$

For the present analysis, the power spectral density has been estimated over data segments of 600 s duration. To define the template lattice, the parameterization using the quality factor $Q_0 = 2\pi\tau_0 f_0$ instead of the duration τ_0 is preferred. Using the algorithm of [38], we tile the parameter space (f_0, Q_0) with a minimal match of 99%. The parameter ranges 150 Hz $\leqslant$ $f_0 \leqslant 2$ kHz and $2 \leqslant Q_0 \leqslant 16$ correspond to the frequency band of best sensitivity for Virgo during the C7 run. This generates 420 templates; the shortest and longest ones have 0.31 ms and 34 ms duration.

The quantity $\rho = \sqrt{2 \times |C|^2}$ is the signal-to-noise ratio (SNR), which we use as a detection statistic. It depends on the analysis time t, the template frequency f_0, and quality factor Q_0. It thus defines a three-dimensional representation map of the data [37] in which we search for a local excess as compared to typical noise fluctuations.

We first apply a low threshold (SNR of 3.3) to the map. We form clusters with the surviving pixels of energy $|C_i|^2$ with a two pass procedure. The pixels are grouped into clusters using the Hoshen–Kopelman algorithm [39]. Once the cluster is formed, all pixels that have a SNR lower than 5 are removed. Then, all clusters overlapping in time or separated by less than 50 ms are grouped together once again. We produce the final list of triggers by requesting that the cluster SNR $\left(\sqrt{2 \times \sum |C_i|^2}\right)$ is larger than 11.3. This choice for the threshold is a good compromise between not having too many triggers and not losing too much detection efficiency.

The triggers' information is extracted from the clusters. The peak time, peak frequency and the trigger SNR are defined by the pixel that has the highest SNR. The duration and the frequency bandwidth of the trigger take into account all the pixels in the cluster. The timing resolution of EGC has been estimated for different kinds of waveforms [37, 40]. For most signals used in the benchmark test, the timing resolution of EGC is smaller than 1 ms for SNR of 10, but it can be as large as a few ms.

3.4. Vetoes

The search for GW burst events presented here was carried out on real data that are non-Gaussian and non-stationary. This prevents the use of theoretical estimates of the expected false alarm rate. In contrast, the background rate must be extracted from the data itself. In the multi-detector context, the background can be estimated by computing the rate of (purely accidental) coincidences between trigger lists that were time shifted with random delays [22, 25]. We cannot resort to such a procedure in the case of this study since we only have the Virgo C7 data set at our disposal. There is a need to initially identify, in an thorough way, all the sources of noise that generate large SNR triggers that can mimic GW burst events; these types of noise events have to be suppressed before we try to estimate the background event number.

We define a methodology that guarantees that we do not discard any true GW event as long as they do not coincide with a bad quality data period. Initially, there was the study of all the sources of noise that generate large SNR triggers, or more generally an excess of triggers, and the construction of vetoes to suppress these triggers. The study was performed on a subset of the C7 dataset (the playground segment) chosen arbitrarily before starting the GW burst

search, in order to avoid bias. Our main concern in the veto development process was to minimize the dead time introduced by the data quality selection, while assuring a high level of noise trigger rejection. To perform the background studies and develop the veto strategy we used the longest C7 science segment; this segment was 14 h in duration (22% of the whole dataset used for the GW burst search).

Several transient detection algorithms (excluding EGC in order to avoid bias) have been applied to the playground dataset to identify and characterize the sources of noise that generate the high SNR triggers that mimic a GW burst event. Mean filter searches for an excess in a moving average computed on whitened data [41]. Peak correlator is a matched filter using Gaussian waveform templates [41]. The wavelet detection filter is based on a multi-resolution time-frequency transform applied on whitened data [5]. Results of these pipelines have been compared to ensure that all sources of transient events have been discovered. These detection algorithms search for a short duration excess of energy, but using different methods. All of the trigger lists show a rather large excess of events compared to expectation from Gaussian noise; there was a definite excess of large SNR triggers.

Two categories of large triggers have been identified; the first one corresponds to short glitches correlated to a glitch also present in an auxiliary channel. These auxiliary channels include the available environmental monitoring and control loop signals (see section 3.4.1). The second category of glitches have been found to be due to the so-called 'bursts of bursts' that we describe in section 3.4.2. Specific vetoes against these two sorts of glitches have been developed as explained in section 3.4.3.

3.4.1. Origin of the short duration glitches. To veto all periods of data during which instrumental or environmental problems occurred and generated a glitch in the GW channel data, one first needs to figure out which auxiliary channels are the most sensitive to these particular sources of noise. The by-eye scanning of the loudest events observed in the playground dataset already gave hints to potentially useful auxiliary channels. However we subsequently performed a systematic analysis using many channels recorded by Virgo and using the mean filter pipeline.

We have found that three channels were particularly interesting for vetoing glitches in the GW strain amplitude channel $h(t)$. It has been seen that many high SNR burst events are coincident in time with the realignment of the quadrant photodiodes by some stepping motors. These quadrant photodiodes, used for the interferometer automatic alignment system, are located at the output of the interferometer, on the same optical bench hosting the photodiodes used to detect the interferometer dark port signal. The stepping motors were generating very loud acoustic and mechanical noise that coupled into the dark fringe beam nearby. Each time a quadrant photodiode is moved there is a large increase in the signal measured by an accelerometer probe located on the detection bench. When the quadrant photodiodes were not re-aligned (horizontal and vertical positions remain constant) the RMS of the accelerometer probe signal remained low. The rate of the quadrant photodiodes' realignment was not constant over the run; initially the alignment occurred every 3 s, but this was then reduced to every 300 s at the end the C7 run after the discovery of the problem (the parameters of the process responsible for the quadrant photodiodes realignment have subsequently been changed to diminish this problem). This acoustic/mechanical noise generated glitches in the GW strain amplitude channel whose frequency content was around 550 Hz. Due to the fact that the excess of acoustic noise could last up to 1 s, which is long for a glitch finding algorithm, we used the RMS computed over 100 ms of data from an accelerometer located on the detection bench instead of the mean filter triggers to create a veto (called 'Seismic' in the writing below). This allowed a more precise definition of the GPS time of the maximum of the excess of

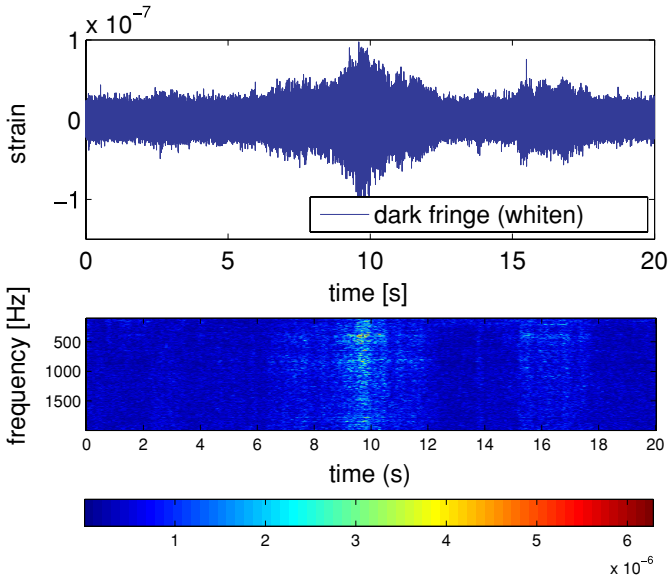

Figure 2. An example of a burst of bursts (BoB) around $t \simeq 10$ s. The upper plot shows the whitened interferometer dark port channel amplitude as a function of time, while the bottom plot is the corresponding spectrogram.

noise. This source of glitches has been found to be dominant in the playground dataset, but other (and rarer) types of glitches have also been found in the C7 data. Indeed, events in the second stage frequency stabilization system correction signal were observed in coincidence with $h(t)$ glitches. Some remaining loud glitches discovered in the GW strain amplitude channel have been found to be coincident in time with a dip in the power of the beam reflected by the interferometer toward the laser as recorded by the so-called B2 photodiode. The light impinging on the B2 photodiode is sensitive to the power-recycling cavity length change. The origin of the power dips have not been understood, but the effect on the GW strain amplitude was demonstrated and the safety of this veto using an optical auxiliary channel has been carefully studied, and is discussed below. To define an event by event veto for the two latest categories of glitches we used the mean filter triggers. These vetoes are hereafter referred to as 'SSFS' and 'B2'.

3.4.2. Bursts of bursts. We noted that the burst triggers were not uniformly distributed over time but seemed to show up in bunches lasting up to a few seconds. These events have been called bursts of bursts (BoB). Figure 2 shows the whitened GW strain channel's amplitude and its spectrogram during a data period that contains a burst of bursts.

The spectrogram shows that the event has a broadband frequency content contrary to most of the events caused by external disturbances. This broadband spectral signature provided clues that helped to identify the BoBs as local increases of the noise level due to an increase of the coupling factor between the frequency noise (which is only a factor 2 lower than the shot noise at high frequency for C7) and the interferometer's dark port channel. The presence of a peak around $T \simeq 27$ s in the correlogram of the burst events (see figure 3) provided evidence that the residual angular motion of the mirrors could be playing a role. Indeed, 27 s corresponds to the period of a mechanical resonance between the two last stages of the Virgo suspension that, if excited, may induce mirror angular degrees of freedom motion [42]. It turns

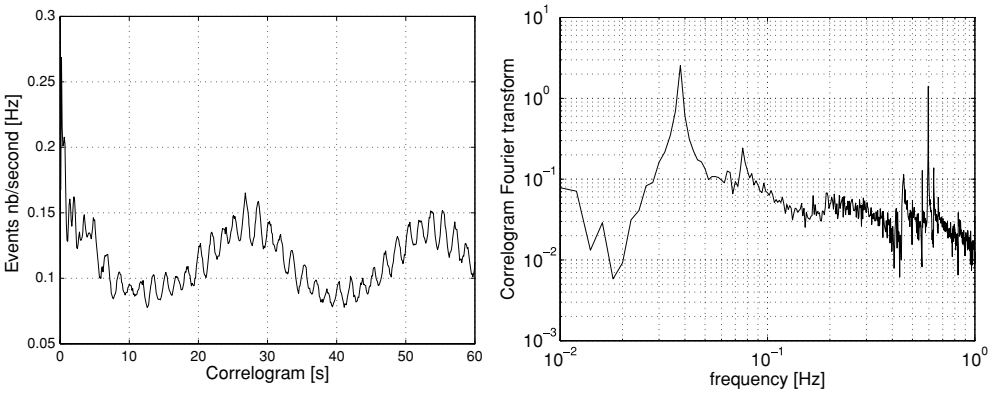

Figure 3. Left: the correlogram of the triggers found by the EGC pipeline in the C7 dataset. A peak around $T \simeq 27$ s is present, with a replica at 54 s. A 0.6 Hz modulation is also visible, and this frequency corresponds to the pendulum mode of the last stage of the Virgo suspension. Right: the Fourier transform of the correlogram. The 37 mHz mechanical resonance between the two last stages of the Virgo suspension is clearly visible.

out that the mirrors' alignment control system was not optimally working during C7 and the angular tilts of the mirrors induced an increase of the coupling of the laser frequency noise with the dark port amplitude. The BoB events represent a rather large fraction of the burst triggers in C7, as can be seen in figure 3, where the number of triggers in the correlogram fluctuates by up to ∼50%. This is also visible by the height and width of the 37 mHz peak in the Fourier transform of the correlogram. The BoBs contribute partly to the highest SNR triggers, but mainly to the moderate SNR values.

These non-stationary noise periods must be eliminated from the analysis since they generate an excess of noise triggers and they correspond to periods where the Virgo sensitivity is degraded compared to the norm. To identify those periods we used the band limited RMS of the dark port channel amplitude around 1111 Hz, which is the frequency of the line injected to measure the laser frequency noise component in the dark port channel. This line allows one to measure the common mode noise level in the GW strain amplitude, and especially the laser frequency noise. Actually, measuring the height of the line allows one to monitor the variation of the common mode coupling factor [43]. We computed the band limited RMS of the dark port channel amplitude around 1111 Hz over 10 Hz (1106–1116 Hz), at a sampling rate of 20 Hz. The high values of the band limited RMS correspond to periods where the non-stationary excess of noise is large. That allowed us to define the '1111 Hz' veto.

3.4.3. Veto parameters tuning. Once the channel and filter have been identified, one needs to tune the parameters of the veto, namely the threshold and the duration of the vetoed window around the time of the glitch. The parameters are adjusted to maximize the veto significance, keeping the dead time (i.e., percentage of vetoed science time) below a reasonable value. The significance is defined as the ratio of the number of triggers (presumed to be instrumental glitches) that the procedure vetoes by the square root of the number of triggers it would accidentally veto if there is no physical link between the glitches of the auxiliary channel and $h(t)$.[17] The significance measures the excess of coincident events in standard deviation units.

[17] The significance $= \frac{N-n}{\sqrt{n}}$ where N is the number of coincidences and n is the estimation of accidental events assuming Poisson statistics.

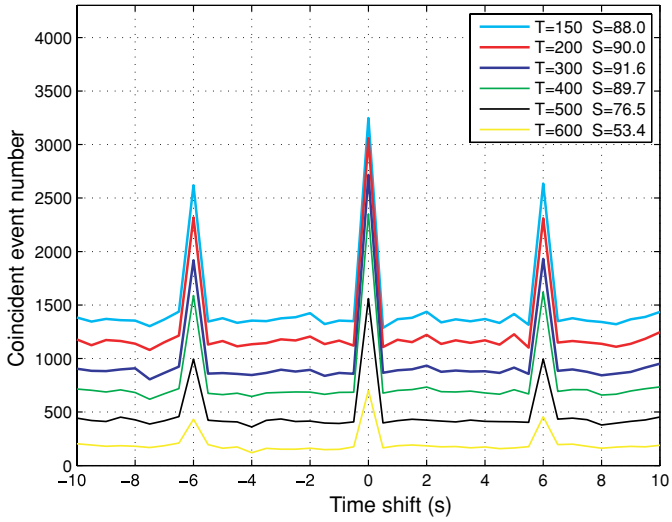

Figure 4. Number of coincident triggers between the GW strain amplitude and the auxiliary channel that has been used to define the Seismic veto, as a function of the time shift introduced in the Seismic veto list. The different curves have been obtained for different threshold values (T). *S* is the significance. The peaks correspond to the stepping motor that have been activated each 6 s during the playground dataset. The different curves have been obtained for various values of the threshold applied on the auxiliary channel RMS. The maximal value of the significance is obtained for a threshold of $T = 300$.

We used the GW strain amplitude triggers of the EGC pipeline to tune the vetoes as we wanted an optimal background rejection for this analysis. The rate of accidental coincidence was measured by artificially time shifting the list of auxiliary glitches while the number of vetoed triggers is obtained for the zero-lag. We vary the threshold on the auxiliary channel output (SNR or RMS) and the duration of the veto window. For each value we compute the dead time, the efficiency (fraction of EGC triggers that are vetoed) and the use percentage of the veto (fraction of auxiliary channel triggers that veto an EGC trigger). A good veto must have a high use percentage [44]. The size of the veto window must be larger than the peak time difference in order to conservatively veto the region around the glitch, and can be as large as the total duration of the auxiliary channel trigger. Values from 100 ms up to 600 ms have been tested.

Figure 4 shows the number of coincident triggers between the GW strain amplitude and the auxiliary channel that has been used to define the Seismic veto, as a function of the time shift introduced in one of the lists. In this case, the auxiliary channel triggers are the RMS of the channel computed at 10 Hz. Different values of the threshold have been tested (from 150 up to 650 by steps of 50). The maximal value of the significance is obtained for a threshold of 300. The threshold is confirmed by the fact that below this value the veto efficiency reaches a plateau. The choice of the duration of the veto window is based on a compromise between a high use percentage and a low dead time for the value of the threshold chosen. We checked that the optimal value, 500 ms, matches the width of the time difference between the auxiliary channel RMS and the EGC triggers.

The same procedure has been applied to tune the parameters of the 'SSFS' and 'B2' vetoes using the playground dataset. Some differences, compared to the Seismic case should be noted. For these two vetoes, built on the triggers generated by the mean filter glitch finding algorithm,

Table 1. Definition and parameters of the four event by event vetoes that have been developed and tuned for this analysis.

Veto	Auxiliary channel quantity	Threshold tuning method	Threshold	time window
1111 Hz	Band RMS (computed at 20 Hz)	Dead time	12	Period above the threshold +/-300 ms
Seismic	RMS (computed at 10 Hz)	Significance	300	500 ms (fixed)
SSFS	SNR of the mean filter triggers	Significance	6	Mean filter trigger duration - minimal value: 300 ms
B2	SNR of the mean filter triggers	Significance	10	Mean filter trigger duration - minimal value: 300 ms

we used the information of the trigger duration to define the veto duration, in addition to a fixed minimal window size. For the 1111 Hz veto, the duration of the window was defined by the time when the band RMS was above the threshold. The veto duration was then symmetrically enlarged. Given the nature of the BoB events (high EGC trigger multiplicity and rather noisy periods) we could not use the significance to optimize the threshold as it leads to setting the threshold at a very low value corresponding to an unacceptable large dead time. Instead, we set the threshold such that the dead time remained below 20%. We checked that this choice assures that the veto was able to suppress a large fraction of the BoB events. The veto definitions and the chosen parameters are reported in table 1.

3.4.4. Veto safety. The safety of a veto is of fundamental importance as we do not want to inadvertently eliminate any real GW event. Vetoes based and dedicated to suppress coincident glitches in the GW strain amplitude channel must be safe with respect to real GW events. The DQ flags and vetoes which suppress deleterious periods of data can be potentially unsafe since the source of noise is independent of the effect of a real GW impinging upon the detector. In contrast, we must be sure that a veto based on an auxiliary channel that has some glitches remains silent when a real GW event is passing through the detector. More precisely, environmental channels such as acoustic or seismic probes are expected to be safe, whereas vetoes constructed on optical or interferometer control channels may be unsafe, since a GW event will generate a change in photodiode signals that can be used within the feedback loop of some control systems. To test the safety of an auxiliary channel, one can examine the periods where hardware injections of fictitious GW signals are inserted into the interferometer. A deterministic force applied on the north input (NI) mirror, induces a variation of the length of the north arm Fabry–Perot cavity which then mimics the effect of a real GW on the interferometer. During C7 there were two periods of hardware injections, and these included two different type of burst waveforms: 60 Sine Gaussian ($f = 920$ Hz, $Q = 15$ and $f = 460$ Hz, $Q = 15$), and 33 Gaussian ($\sigma = 1$ ms). Both of these signals were injected with a SNR of 15 using a sensitivity curve taken just before the run started (the real SNR of the hardware injections is somehow different due to the sensitivity variation during the run). The critical point concerns the safety of the SSFS and B2 vetoes, which could in principle be unsafe. None of the hardware injection signals have been vetoed by the Seismic, SSFS and B2 vetoes. This establishes that our vetoes were safe. The anti-BoB veto 1111 Hz which was built using directly the gravitational wave channel was, by construction, unsafe for GW burst event whose frequency content is around 1111 ± 5 Hz. We could not check that the veto was unsafe for these signals using the hardware injections as no signal with enough amplitude in this frequency range has been injected, but we should consider that the GW burst analysis

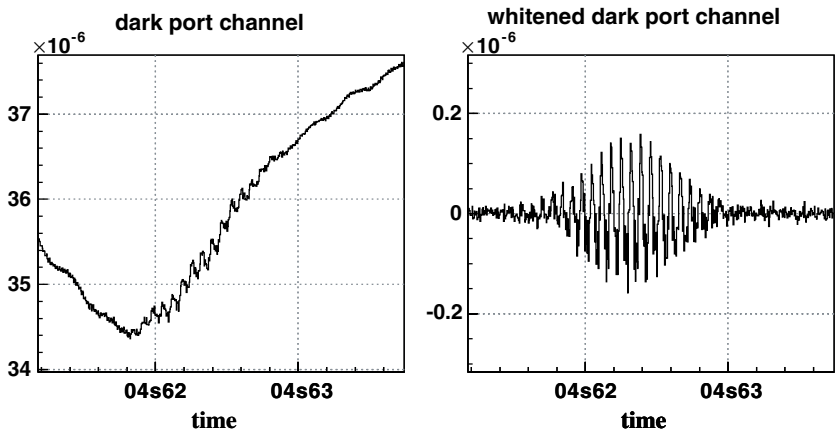

Figure 5. Time series in the dark port channel (left) and the whitened dark port channel (right) of the loudest event detected by the EGC pipeline in the search for GW bursts in the C7 data. This event was seen with a SNR of 69.7 at a frequency about 1466 Hz.

presented here is insensitive for GW signals in the 1106–1116 Hz frequency band. Besides, the safety of a veto assumes that its dead time remains small. This is the case for all the vetoes used in this analysis except the 1111 Hz veto whose large dead time (16.1%) might suppress a real GW burst event. The anti-BoB veto 1111 Hz suppressed two hardware injections, which is less than what we could foresee given the large dead time of this veto.

4. Output of the GW burst search pipeline

4.1. First results

We have generated the veto lists for the full C7 data set applying the tunings that have been defined using the playground segment as explained in section 3.4.3. After applying the vetoes on the whole dataset, the remaining largest SNR triggers were studied in order to assess their compatibility with a GW burst signal. At this stage, we ended up with a single rather large SNR event that has been subsequently thoroughly studied. This very peculiar event has been observed outside the playground segment. Only one event of this type has been found in the full run, at least with such a SNR. It looks like a Sine Gaussian signal, as shown in figure 5, with a SNR of 69.7, for one of the Sine Gaussian templates ($f = 1466$ Hz, $Q = 15.5$, $\sigma = Q/\Pi f =$ 3.4 ms); all environmental channels have been checked around this period using different glitch finding algorithms. Nothing suspected was found in any of the channels. However, the event was visible in the other phase of the demodulated dark port signal. We concluded that this event could not have been generated by a GW burst, but more likely could be due to an experimental problem, not occurring in the chosen playground segment. Indeed, the modulation phase angle was tuned such that the effect of a GW crossing the interferometer was contained in one demodulated phase (ACp) of the dark port signal, while the other (ACq) should not be perturbed. This observation lead us to develop an event-by-event veto (called 'PQ') based on the ratio of the SNR of time coincident triggers in the two demodulated phase signals as proposed in the literature [45–47]. Despite the fact that such a kind of events have not been found in the playground segment as a significant source of loud noise events, we

decided to develop this veto and to apply it on the full data set. The other loudest high SNR events have been found compatible with BoB-like events.

4.2. Necessity of an a posteriori veto

The in-phase signal contains *a priori* the GW strain amplitude, provided that the demodulation phase is well tuned. An error in the demodulation phase induces a small coupling of the GW signal with the quadrature channel. However, the ratio of the GW energy seen in the two phases is expected to remain high. The ratio is expected to be proportional to $\frac{1}{\sin(\delta\phi)}$, where $\delta\phi$ is the error on the demodulation phase [46]. Unfortunately we do not know precisely the value of $\delta\phi$ during C7. A real GW event will be seen with a SNR in ACp much higher than in ACq. In contrast, ACq will be sensitive to glitches in signals which are related to common mode noise. It may happen that some source of noise can affect both quadrature signals with similar strength. This is especially the case for a dust particle crossing the laser beam before the output dark port photodiode where the beam is especially small in width. A key point of such a veto is to assure that no real GW events would be suppressed, and therefore one would need to develop a veto with a rather good security factor. To do so, we used the hardware injections to verify safety and develop the characteristics of this veto.

EGC triggers have been generated for the dark port ACp and ACq channels and all events with SNR above 5 were considered. We then required time coincidence between the two sets of triggers using a window of ± 10 ms. No coincidence in frequency has been required. The hardware injection signals were detected in the ACp triggers with an efficiency of 98%. Unfortunately during C7, the injected SNR was not, on average, very large and consequently the signal energy in the ACq channel could not be expected to be very high (below the pipeline threshold at SNR = 5). Among the 91 detected hardware injections only five had a coincident trigger in the ACq phase channel within 10 ms; this tends to indicate that a large fraction of the GW energy would be contained in the ACp channel as expected; this is displayed in figure 6. The ratio between the SNR detected in the two demodulation phase channels in coincidence is

$$\kappa = \frac{\mathrm{SNR}_{\mathrm{ACp}}}{\mathrm{SNR}_{\mathrm{ACq}}}. \tag{4}$$

The very low event statistics (five events detected simultaneously in ACp and ACq) encourages us to stay conservative when defining the PQ veto parameters. We checked that the use of a ± 10 ms window limits the accidental coincidence event rate to 0.2 over the period of the hardware injections (assuming a Poisson trigger rate). This excludes the fact that we have more than one accidental association with an ACq trigger for the fix burst hardware injections as shown in figure 6. In this figure, the strange and unique high SNR event is totally isolated from the rest of the events. This event has $\kappa \simeq 0.42$ and a SNR in the ACq channel of 141; these facts totally exclude the possibility that this event has been generated by a real GW.

The goal of the PQ veto is to suppress high SNR events in the ACq channel that induce a transient in the dark port channel amplitude. That is why it is reasonable to consider only large SNR ACq triggers. A threshold is applied on the SNR of the ACq triggers ($\mathrm{SNR}_{\mathrm{ACq}}$). The other veto parameter threshold pertains to the ratio κ. We did not try to optimize these two parameters, but rather we keep a conservative attitude with respect to the hardware injection signals' position in the two-dimensional plane that shows the SNR of both quadratures for the coincident triggers (see figure 6). The veto list segments have been defined as the periods during which $\mathrm{SNR}_{\mathrm{ACq}} > 8$ and $\kappa < 1$. All burst hardware injection signals pass these conditions with a safety factor since they are all below the $\kappa = 2$ line. The starting and ending

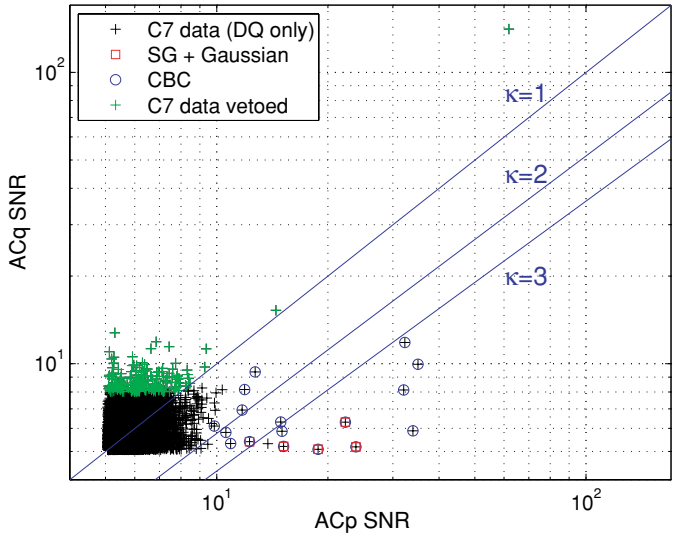

Figure 6. SNR of the coincident EGC triggers in the two quadrature demodulated channels of the output dark port signal: ACp (in phase) and ACq (in quadrature). The time coincidence window of the triggers seen in the two channels is 10 ms. The Seismic, SSFS, B2 and 1111 Hz vetoes have already been applied. The peculiar event appears very isolated with respect to the other triggers with its ACq SNR of 141. The hardware injection signals, which were seen in both of the two demodulation phase channels, are indicated by the circles for burst-like signals and by the squares for the compact binary coalescence (CBC) signals.

Table 2. Dead time of the different vetoes that have been found useful. The values are computed for the full C7 dataset.

Veto name	Seismic	SSFS	B2	PQ	1111 Hz	All vetoes
Dead time	3.75%	2.6%	0.03%	0.07%	16.1%	21.2%

times of the veto segments are given by the ACq trigger times. The dead time of the PQ veto is 0.07%, which is very acceptable.

4.3. Final results

Table 2 gives the dead time of the five event-by-event vetoes which have been used in this analysis. The total dead time amounts to 21.2% taking into account overlapping veto segments. This is a rather high value, mainly because of the presence of the non-stationary excess of noise due the looseness of the mirror's angular degree of freedom control during C7.

Figure 7 shows the triggers' SNR distribution obtained from the full C7 data set, after having applied consecutively the five vetoes (note that the highest SNR event is off of the scale of the plot). The four anti-glitch vetoes (Seismic, SSFS, B2 and PQ) suppress 10.6% of the total number of triggers and play an important role for the large SNR (>10) events since 51.3% of them are eliminated. The anti-BoB veto is critically important, and its efficiency on EGC triggers is impressive; 45.6% of the remaining triggers are eliminated, and 97.6% of the remaining loudest ones (SNR >10). Figure 8 shows the SNR of the remaining triggers as a function of their frequency. The application of all these vetoes allows us to reduce, by

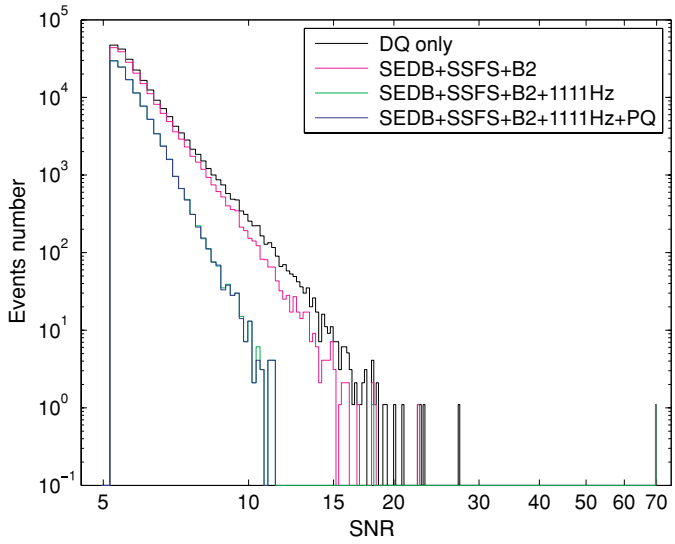

Figure 7. SNR distribution of the triggers obtained on the GW strain amplitude channel by EGC after applying all vetoes on the full C7 data set.

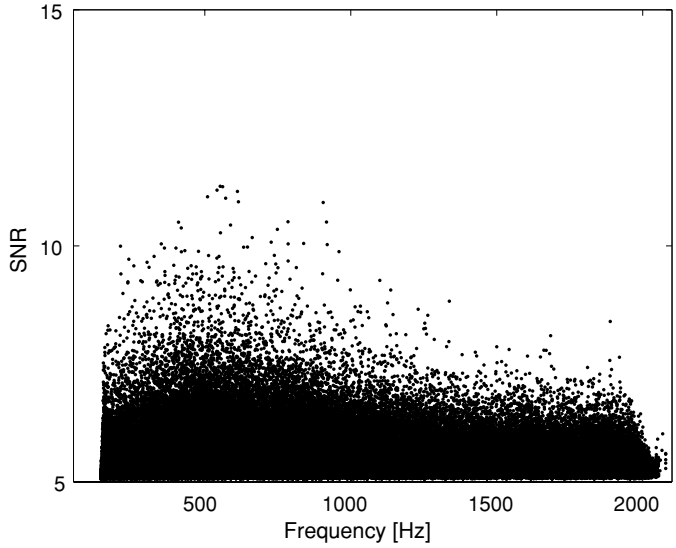

Figure 8. SNR as a function of the frequency of the triggers obtained on the GW strain amplitude channel by EGC after applying all vetoes on the full C7 data set. The distribution around 2 kHz is due to the templates' placement; some Sine Gaussian templates have a central frequency which can slightly exceed 2 kHz.

a factor 2, the number of events for all EGC triggers above SNR = 5. 98.8% of the EGC events above SNR >10 were eliminated. 21 triggers above SNR = 10 remain at the end. The loudest has a SNR of 11.26, and although it was not vetoed, it seems to be due to a short period non-stationary Virgo noise increase. We have determined that it is not a gravitational

wave event, but rather a BoB event. It has the same frequency content as the BoB events but its amplitude was not large enough to be suppressed by the anti-BoB veto.

5. GW burst search analysis sensitivity

5.1. Generation of the injected waveforms

The GW burst search presented in this paper is intended to be efficient for all waveforms as long as they have energy concentrated in time and frequency in the range 150–2000 Hz. However, since the Virgo sensitivity is not constant over this frequency band, the detection efficiency for a given signal strength will depend on the frequency of the signal. In order to assess the sensitivity of the detector to dissimilar kinds of signals at different frequencies, we used simulated waveforms of diverse types. These were added to the Virgo GW strain amplitude (software injection) and analyzed by the EGC pipeline, similar to how the C7 triggers were produced. These injected signals were randomly distributed in time during the C7 run, assuring a minimal separation of 60 s [48].

The waveforms investigated in this analysis were of two types. One group consisted of ad hoc waveforms, such as Sine Gaussians and Gaussians, whose detection efficiency is expected to depend mainly on the central frequency, bandwidth and duration of the waveform. On the other hand, to test the efficiency of this analysis to detect BBH merger and ring-down GW signals we used waveforms provided by numerical relativity simulations [49]. We also used a signal pertaining to a star core collapse, referred to as A1B2G1, from the supernova simulation catalog available in [50].

The amplitude of the GW associated with an astrophysical source depends on the distance of the source from the Earth. To quantify the strength of a GW burst, we used the root sum squared of the strain amplitude at the earth without folding in the detector antenna pattern

$$h_{rss} = \sqrt{\int (|h_\times(t)|^2 + |h_+(t)|^2)\,\mathrm{d}t}, \tag{5}$$

where h_+ and $h_\times$ are the two GW polarizations that we express below for the different cases relevant to our analysis. For a binary BH waveform h_{rss} is computed assuming a null inclination angle for the orbital plane.

5.1.1. Sine Gaussian and Gaussian waveforms. For the Sine Gaussian and Gaussian signals, the detection efficiency is expected to depend mainly on the central frequency, bandwidth and duration of the waveform. For these signals the strain sensitivity $h(t)$ of the detector can be written as

$$h(t) = F_+(\theta, \phi, \Psi)h_+(t) + F_\times(\theta, \phi, \Psi)h_\times(t), \tag{6}$$

where $F_\times$ and F_+ are the antenna response functions characterized by the source position (θ, ϕ) and polarization angle Ψ relative to the detector [51]. Specifically, for Sine Gaussian injections we used circular polarized waveforms described by

$$h_\times(t) = h_0\,\mathrm{e}^{-2(\pi f_0 t/Q_0)^2}\sin(2\pi f_0 t), \qquad h_+(t) = h_0\,\mathrm{e}^{-2(\pi f_0 t/Q_0)^2}\cos(2\pi f_0 t). \tag{7}$$

The typical duration of a Sine Gaussian signal depends on the parameter Q_0 and the central frequency f_0 as $\frac{Q_0}{2\pi f_0}$. Several values of f_0 ranging from 100 Hz up to 1797 Hz and $Q_0 = 3$, 8.9 and 9 were used. Their narrow-band feature allows the testing of the pipeline performance in a given frequency region.

For Gaussian injections, we used linearly polarized waveform given by

$$h_+(t) = h_0\, \mathrm{e}^{-t^2/\tau^2}, \tag{8}$$

$$h_\times = 0, \tag{9}$$

where τ is the width of the signal. Gaussian waveforms are of interest in the GW burst search because many predicted signals associated with core collapse GW emission just after the bounce have large peak structures. We chose the values of τ to lie between 0.1 and 6 ms. In the case of linearly polarized Gaussians, the angles θ, ϕ have been randomly chosen. For the circularly polarized Sine Gaussians the randomization has been done over the angles θ, ϕ and Ψ.

5.1.2. Astrophysical waveforms. For the core collapse signals, we have chosen only one waveform produced by a core collapse 3D simulation conducted with numerical general relativistic techniques in order to estimate, with a physical model, the detection efficiency for a realistic supernova GW signal. This signal corresponds to the case of a stiff equation of state, a small initial differential rotation and a moderate rotational kinetic energy [50]; this leads to a waveform with a large negative peak followed by a ring-down phase (regular collapse). More up-to-date simulations [52–54] using hydrodynamical models with realistic nuclear equations of state, deleptonization and progenitor models from stellar evolutionary calculations tend to confirm the general features of the regular core collapse. In this present study we are not interested in the details of the waveform. The waveform is linearly polarized and the simulations have been done similarly to the Gaussian signals.

With the recent breakthroughs in the field of numerical relativity (NR), many groups have been able to simulate the evolution of binary BHs through three stages: inspiral, merger and ring down [14, 49, 55]. These waveforms have been shown to be consistent with the already existing analytical results using post-Newtonian and BH perturbation theories [56–59] for the inspiral and ring-down phases, respectively. Furthermore, despite the differences in the numerical methods employed, gauges chosen, and methods adopted to evolve the systems, qualitatively the results from all groups show good agreement [60]. All these provide a motivation to use these results from a data analysis perspective. Many such attempts have already been made to search the three phases of the binary black hole evolution using NR outcomes [56, 61, 62]. We apply these results from the point of view of a GW burst data analysis and use the NR waveforms to assess the efficiency of the EGC burst pipeline to detect the BBH merger. For this application we used the numerical relativity (NR) simulations of the non-spinning, equal mass BBHs provided by the Goddard Space Flight Center group [49]. The injected waveforms were GW strains from the leading $l = 2$, $m = 2$ spin-weighted spherical harmonics from the simulations. These waveforms had (approximately) three cycles of inspiral, followed by merger, and then a ring down.

Unlike the ad hoc waveforms or the linearly polarized case of SN waveforms, one has to include the effect of the orbital inclination angle ι for the BBH merger waveforms. Equation (6) should be rewritten in order to include the effect of orbital inclination as

$$h(t) = F_+(\theta, \phi, \psi)A_+(\iota)h_+(t; \iota = 0) + F_\times(\theta, \phi, \psi)A_\times(\iota)h_\times(t; \iota = 0), \tag{10}$$

where F_+ and $F_\times$ are the usual antenna pattern functions, $A_+ = -\frac{1}{2}(1 + \cos^2 \iota)$, $A_\times = -\cos \iota$ and $h_+(t; \iota = 0)$ and $h_\times(t; \iota = 0)$ are the polarizations for the situation of zero inclination angle ι. In this case, the simulated waveforms are generated by randomizing all four angles involved. The NR waveforms for the BBH mergers in the total mass range 5 $M_\odot$–150 $M_\odot$ were injected into the C7 data in order to calibrate the detection efficiency of the pipeline to these types of mergers. The range of masses chosen for the injection was decided in accordance with the sensitivity of the C7 run.

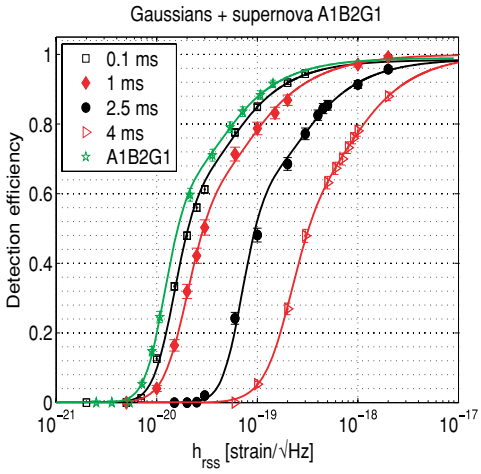

Figure 9. Detection efficiency of the search analysis as a function of the signal strength h_{rss} at earth for the Gaussian waveforms (with τ specified in the legend) and one core collapse simulated waveform (A1B2G1). The efficiencies were computed for sources at random sky locations. The error bars take into account only the statistical error on the detection efficiency.

5.2. Detection efficiency of the GW burst search with the software injections

We applied the same data quality criteria (DQ and vetoes) on the trigger list containing the waveform injections. The detection efficiency is defined as the fraction of injected signals reconstructed with a SNR larger than 11.3 corresponding to the loudest event found in the C7 data triggers. As the veto dead time is rather large, the vetoed periods have not been considered when computing the detection efficiency. Figures 9, 10 and 11 show the detection efficiency as a function of h_{rss} for each family of waveforms. The error on the efficiency data points takes into account only the statistical error. To estimate the values of h_{rss} at efficiency 50% and 90% the four parameters of an asymmetric sigmoid function have been fitted to the data points. The efficiency $\epsilon(h_{rss})$ is defined as follows:

$$\epsilon(h_{rss}) = \frac{\epsilon^{\max}}{1 + r^{\mathrm{mid}\,\alpha(1+\beta\tanh(r^{\mathrm{mid}}))}}, \tag{11}$$

where $\epsilon_{\max}$ is the maximal efficiency obtained for strong signals (it should tend to unity). r^{mid} is the ratio $h_{rss}/h_{rss}^{\mathrm{mid}}$ where h_{rss}^{mid} is the strain amplitude at half height, i.e., we have $\epsilon\left(h_{rss}^{\mathrm{mid}}\right) = \epsilon^{\max}/2$. α and β are respectively the slope and the asymmetry of the sigmoid function. The parameters were estimated by minimizing a χ^2 function. $\epsilon^{\max}$ is constrained to remain smaller than unity. For signals for which $\epsilon^{\max}$ does not reach unity, we checked that this is due to a fraction of signals with an injected SNR smaller than the threshold of 11.3. This is especially the case for the Gaussian and the A1B2G1 core collapse simulated waveforms, as expected. Indeed, as the frequency content of the Gaussian signals is maximal at low frequency, for a fixed h_{rss} and a random sky position, we expect a non-negligible fraction of low SNR Gaussian signals.

As expected for the Gaussian signals, the performance decreases as the width τ of the Gaussian increases. For τ greater than 4 ms, the detection efficiency is already quite poor, as shown in figure 9. Note that the results obtained for the supernova signal A1B2G1 are very similar to the Gaussian with $\tau = 0.25$ ms (see table 4); this is not surprising as the

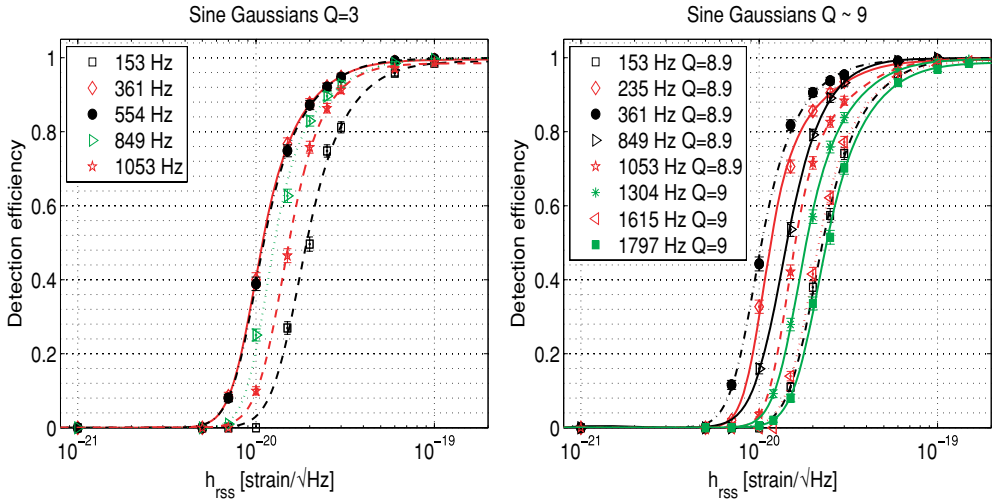

Figure 10. Detection efficiency of the search analysis as a function of the signal strength h_{rss} at earth for Sine Gaussian waveforms with different central frequencies f_0 and for two different values of the Q_0 factor: left $Q_0 = 3$, right $Q_0 \sim 9$. The efficiencies were computed for sources at random sky locations. The error bars take into account only the statistical error on the detection efficiency.

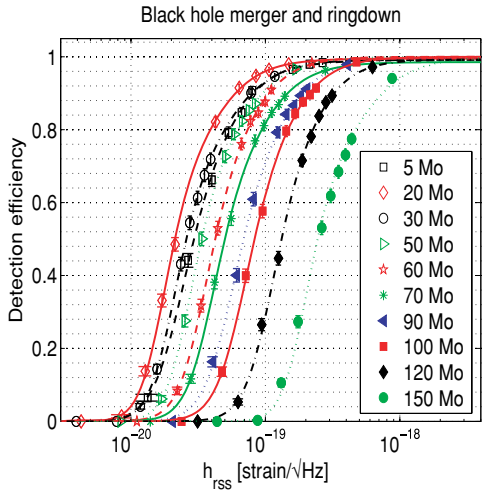

Figure 11. Detection efficiencies from the search analysis as a function of the signal strength h_{rss} for the BBH merger and ring-down waveforms for different BH total masses (but where the two individual component masses are equal). The efficiencies were computed for random polarization, inclination angles and sky positions. The error bars take into account only the statistical error on the detection efficiency.

A1B2G1 signal has a large amplitude peak whose width is approximately 0.35 ms. Figure 10 shows the detection efficiency of the analysis obtained with the Sine Gaussian waveforms; the performance follows the trend of the C7 Virgo noise floor shown in figure 1, which is expected for a signal well localized in frequency, such as a Sine Gaussian.

Table 3. h_{rss} corresponding to 50% and 90% efficiency in units of 10^{-20} strain $\mathrm{Hz}^{-1/2}$ obtained for the ad hoc Sine Gaussian waveforms. The efficiencies were averaged over the full C7 data set for random sky positions. The symbol—means that no simulated waveforms were available. The symbol (*) indicates that we used simulated waveform with $Q = 9$ instead of 8.9.

	50% efficiency		90% efficiency	
f_0 (Hz)	$Q = 3$	$Q = 8.9$ or 9	$Q = 3$	$Q = 8.9$ or 9
100	4.5	10.6	9.1	21.7
153	1.9	2.3	3.9	4.6
235	1.2	1.2	2.3	2.5
361	1.1	1.0	2.2	2.0
554	1.1	1.1	2.3	2.3
849	1.3	1.4	2.6	2.6
945	–	1.5(*)	–	2.9(*)
1053	1.5	1.6(*)	2.8	3.6(*)
1172	–	1.8(*)	–	3.6(*)
1304	–	1.8(*)	–	3.8(*)
1451	–	1.9(*)	–	3.7(*)
1615	–	2.2(*)	–	4.5(*)
1797	–	2.4(*)	–	5.1(*)

The performance obtained for the BBH merger waveforms for a total mass M from 5 $M_\odot$ up to 150 $M_\odot$ (displayed in figure 11) were not as good as for the Sine Gaussian signals. The best $h_{rss}^{50\%}$ was achieved for $M = 20M_\odot$ with $h_{rss}^{50\%} \simeq 2.2 \times 10^{-20}$ $\mathrm{Hz}^{-1/2}$. That was at least two times worse than the best Sine Gaussian result. The merger frequency can be approximated by the empirical formula [13, 25], deduced from figure 8 in [63]

$$f_{\mathrm{merger}} \simeq \frac{15\mathrm{kHz}}{M}, \tag{12}$$

where M is the mass (in units of solar mass) of the final BH formed after merger. M is smaller than the sum of the initial BH masses. For $M = 20$ $M_\odot$ this corresponds to 750 Hz, which is well inside the frequency range of the search. In contrast, for masses above 100 $M_\odot$, f_{merger} is smaller than 150 Hz, which is the lower frequency boundary of this search. The EGC pipeline for this kind of waveform is still able to catch the ring-down part of the signal, which has an appreciable contribution to the SNR, while the performance for a Sine Gaussian at the f_{merger} frequency would hardly be detectable. For the low mass signal the drop of performance is explained by the fact that the frequency at the merger exceeds the upper frequency boundary of this search, and moreover, the equivalent Q is expected to be larger than 16 (the upper value chosen in this search).

The value of h_{rss} corresponding to 50% and 90% of efficiency ($h_{rss}^{50\%}$ and $h_{rss}^{90\%}$) have been determined using the fitted sigmoid functions and are given in tables 3, 4 and 5 for Sine Gaussians, Gaussians, Supernova and BBH merger signals, respectively. The best value of $h_{rss}^{50\%}$, 1.05×10^{-20} $\mathrm{Hz}^{-1/2}$, was obtained with the Sine Gaussian of frequency $f_0 = 361$ Hz and $Q_0 = 9$; this signal is 15 times higher than the noise floor at this frequency. Note that bad performance obtained for the 100 Hz Sine Gaussian is expected since the lower frequency range of the search was 150 Hz. Moreover the C7 sensitivity is quite poor below 150 Hz.

The quality of the fitting procedure has been controlled by checking that χ^2 of the fitting function remains close to unity within at maximum a factor 3. Increasing the error on the efficiency by up to a factor 3 does not change the result on h_{rss} to within 1%. The statistical error on $h_{rss}^{50\%}$ and $h_{rss}^{90\%}$ have been computed using the covariance matrix of the efficiency

Table 4. h_{rss} corresponding to 50% and 90% efficiency in units of 10^{-20} strain $\mathrm{Hz}^{-1/2}$ for the Gaussian waveforms of different widths and one core collapse simulated waveform (A1B2G1). The efficiencies were averaged over random sky position.

τ (ms)	50% efficiency	90% efficiency
0.1	2.1	15.9
0.25	1.8	11.6
0.5	1.8	12.7
1.0	2.9	24.4
2.5	9.6	79.0
4.0	32.4	242.0
A1B2G1	1.63	12.4

Table 5. h_{rss} corresponding to 50% and 90% efficiency in units of 10^{-20} strain $\mathrm{Hz}^{-1/2}$ for the BBH numerical relativity waveforms. The total mass of the system varies from 5 $M_{\odot}$ up to 150 $M_{\odot}$.

Total mass ($M_{\odot}$)	50% efficiency	90% efficiency
5	3.0	8.2
10	2.3	5.6
20	2.1	6.0
30	2.6	7.9
40	3.0	8.0
50	3.4	9.6
60	4.2	10.7
70	5.0	14.6
80	5.8	14.8
90	6.9	18.7
100	8.3	21.3
120	13.2	32.4
150	24.5	74.4

curves; for the Sine Gaussian and BBH waveforms the error on $h_{rss}^{50\%}$ was below 1.3%. Note that for $h_{rss}^{90\%}$ the errors were higher, between 6% and 13%. For the Gaussian and core collapse waveforms the uncertainty is on average larger, indicating that the quality of the fitting was worse. The errors are between 1% and 4% for all the Gaussians, except for the Gaussian with $\tau = 4$ ms for which the error on $h_{rss}^{50\%}$ reaches 11%. However, the biggest uncertainty on the $h_{rss}^{50,90\%}$ values comes from the error on the GW strain ampliude calibration, which is of 40%. Including the systematic error due to the calibration uncertainty leads to an error on $h_{rss}^{50,90\%}$ between 40% and 43%.

6. Search results

6.1. Event rate and GW strength upper limits

From section 4 we can assert that we have not observed any GW event with a SNR above 11.3, corresponding to the loudest event SNR. Knowing the detection efficiency as a function of the signal strength for different kinds of signals, we can now derive a 90% confidence level (CL) upper limit on the event rate that depends on the strength of the signal. Using the loudest

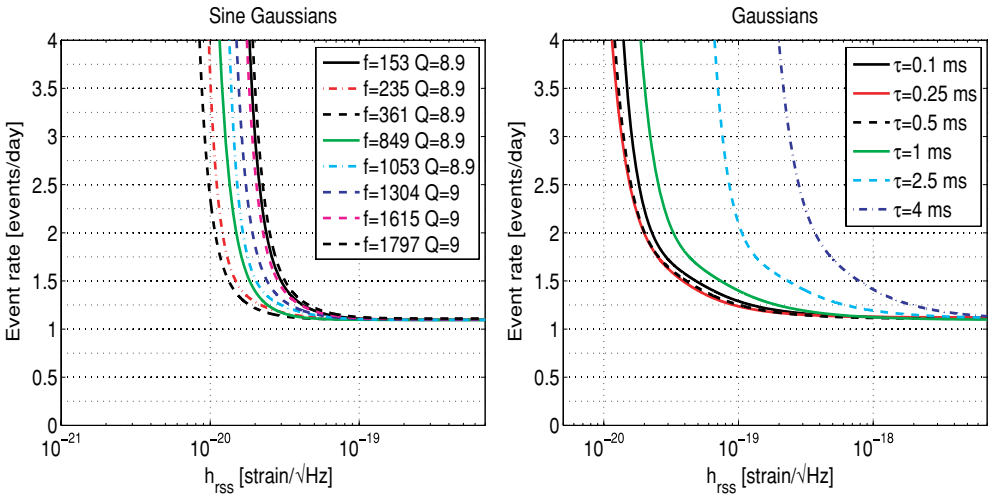

Figure 12. Event rate as a function of the h_{rss} exclusion plots at 90% confidence level obtained in the Virgo C7 data. The left plot corresponds to GW burst events that can be modeled by a Sine Gaussian with a Q of 8.9 or 9 for frequencies, f, covering the most promising part of the C7 frequency range. The right plot corresponds to GW burst events that can be modeled by a peak of different widths, τ, from 0.1 ms up to 4 ms.

event statistic as described in [64], the 90% CL exclusion on the event rate of a signal detected with an efficiency of $\epsilon(h_{rss})$ is given by

$$\mathcal{R}^{90\%}(h_{rss}) = \frac{-\ln(1-0.9)}{T\epsilon(h_{rss})}, \tag{13}$$

where $T \simeq 2.1$ days is the effective observation time for the C7 run (veto times have been subtracted from the total analyzed time). The results are given in figure 12 for the Sine Gaussian waveforms (Q $\sim$ 9) and the Gaussian waveforms.

As expected for strong signals, the exclusion rate reaches the asymptotic value of $\frac{-\ln(1-0.9)}{T} \simeq 1.1$ events per day whatever the signal type. We can exclude at 90% confidence level a GW event rate $\mathcal{R}_{90\%}$, assuming 100% detection efficiency, of 1.1 events per day for $T \simeq 2.1$ days of observation. On the other hand, depending on the characteristics of the signals the exclusion rate, when the signal becomes weak, is rather different. The vertical asymptotic value in figure 12 gives an indication of how the sensitivity of the search depends on a given frequency for the Sine Gaussian, or on the width of the Gaussian waveform. The exclusion results for Sine Gaussian waveforms with $Q = 3$ (from 153 Hz up to 1053 Hz only) are very similar to the Sine Gaussian results with $Q = 9$.

6.2. Astrophysical interpretation

In the previous section we determined the sensitivity of the C7 data analysis to different potential GW burst sources in terms of h_{rss}. This can be translated into an astrophysical estimate on the amount of GW energy emitted by a source or the distance reach, depending on the type of sources we consider. For simplicity we have assumed in our ad hoc waveform simulations that the emission is isotropic, although this may not be the case for a real

astrophysical signal. In the case of a Sine Gaussian waveform with a central frequency f_0 and quality factor $Q \gg 1$, one obtains for the GW energy emitted by the source [65, 66]

$$E_{\rm GW} \simeq \frac{r^2 c^3}{4G}(2\pi f_0)^2 h_{\rm rss}^2, \tag{14}$$

where r is the (non-cosmological) distance to the source. Similarly, for a Gaussian waveform, the emitted GW energy is

$$E_{\rm GW} \simeq \frac{r^2 c^3}{4G}\frac{1}{\tau^2} h_{\rm rss}^2, \tag{15}$$

where τ is the width of the Gaussian.

The above expressions can be used to derive an astrophysical sensitivity with the present C7 data analysis in different ways. For sources at a fixed distance, an estimate on the emitted GW energy can be obtained by using the smallest value of $h_{rss}^{50\%}$. Conversely, if we know the energy emitted in GWs, this information can be used to infer the maximum distance up to which such an event could have been observed by Virgo with an efficiency larger than 50%. In what follows we discuss these various possibilities, quantifying the detectability of supernova events and BBH merger events where the nature of waveforms and the energy of emission are known through the numerical simulations.

6.2.1. Detectability of an arbitrary burst GW event close to the galactic center. Considering the Sine Gaussian and Gaussian waveforms that give the best results in terms of $h_{rss}^{50\%}$, we can compare the estimation of the maximal GW energy emitted by a hypothetical GW burst source in the vicinity of the galactic center, assuming a distance of 10 kpc. With the 361 Hz Sine Gaussian we obtained $h_{rss}^{50\%}$ of 1.05×10^{-20} Hz$^{-1/2}$, which translates into an energy of $\sim 3 \times 10^{-5} M_\odot c^2$. For a Gaussian waveform, the most favorable case corresponds to $\tau = 0.25$ ms and $h_{rss}^{50\%} \simeq 1.79 \times 10^{-20}$ Hz$^{-1/2}$; the associated energy is $\sim 2.8 \times 10^{-4} M_\odot c^2$. Hence the most optimistic limit on the energy differs almost by an order of magnitude between the Gaussian and Sine Gaussian waveforms, while the detection performance in terms of h_{rss} is only two times worse for a Gaussian with respect to a Sine Gaussian.

6.2.2. Detectability of supernova events. We now consider the predictions on the GW energy produced by the collapse of a stellar iron core to form a neutron star. It is assumed that the progenitor star rotates fast enough to generate sufficient deformation. We do not consider here the GWs generated after the core collapse by the development of an oscillation of the proto-neutron star lasting a few hundred of milliseconds [10] since we did not expand the search for corresponding high Q oscillating signals. A few hundred of milliseconds at a frequency around 700 Hz corresponds to a Q of a few hundred. Using the core collapse waveform A1B2G1 injected into the data to determine the efficiency for that particular signal, we can derive the distance reach corresponding to 50% of efficiency as we do for the BBH waveforms; the distance is 0.15 kpc. However, this waveform might not be representative of the overall core collapse bounce waveforms. Indeed, depending on the progenitor model parameters (mass, rotation rate, equation of state) the GW energy prediction can vary by several orders of magnitude [53]: $3 \times 10^{-10}\ M_\odot\ c^2 < E_{GW} < 7 \times 10^{-8}\ M_\odot\ c^2$ with a peak frequency which can be as high as 800 Hz. However, these recent simulations [53] seem to indicate that the waveforms are rather generic regardless of the dynamic of the collapse (pressure dominated or centrifugal bounce). Even in the case of centrifugal bounce, the waveforms exhibit a positive pre-bounce followed by a negative peak, but the typical frequency is lower than in the case of a uniform differential rotation for which the typical frequency is around

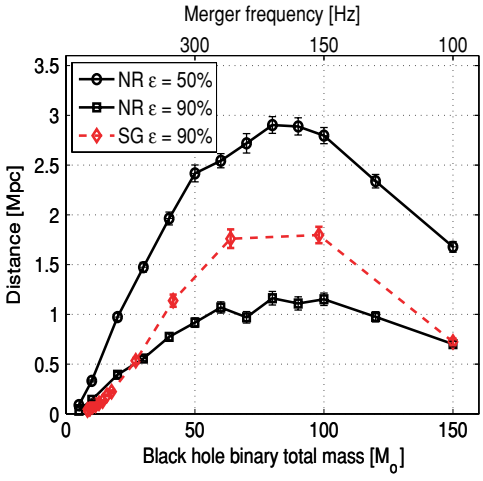

Figure 13. Detection distance of the black hole binary source with efficiency of 90% and 50% as a function of the total mass of the system. The curves with circles and squares have been obtained by estimating the EGC pipeline detection efficiency to numerical relativity black hole binary waveforms. The curve with diamonds was derived from the results obtained with Sine Gaussian waveforms assuming that the waveform when the two black holes merge resembles a Sine Gaussian. The error bars take into account only the statistical error on the detection efficiency.

700 Hz. For instance, if one considers the model with a 20 $M_\odot$ progenitor mass, a moderate differential rotation value ($A = 1000$ km) and a moderate initial rotation rate ($\beta = 0.5\%$) [53], $E_{GW} \simeq 2.32 \times 10^{-8}\ M_\odot$ and the characteristic frequency is 715 Hz using the equation of state provided by Shen [67]. We should not specifically assume that supernova GW signals are monochromatic waveforms like Sine Gaussians. They do not look like Gaussians either (they are more localized in frequency than Gaussian). Taking the $h_{rss}^{50\%}$ value for the $\tau = 0.5$ ms Gaussian (that roughly corresponds to the width of the peak of the considered waveform), we obtain a maximal distance range of 0.18 kpc. Using the Sine Gaussian expression, and using the $h_{rss}^{50\%}$ for a central frequency 715 Hz we obtain a distance of 0.12 kpc. For the A1B2G1 waveform used in this paper, and considering a radiated energy of $E_{GW} \simeq 2.13 \times 10^{-8}\ M_\odot\ c^2$ computed using equation (5) of [7], we obtain a distance of 0.12 kpc whatever the assumption made on the waveform (Gaussian of $\tau = 0.35$ ms or a Sine Gaussian of $f_0 = 650$ Hz). These numbers indicate the order of magnitude of the maximal detection distance we have reached during Virgo's C7 run. This achieved distance is somewhat small, and we expect to gain at least one order of magnitude with Virgo data acquired during more recent observation runs.

6.2.3. Distance reach for binary black hole mergers. From the detection efficiency results obtained with the BBH waveforms in section 5.2, one can derive a distance at which EGC is able to detect a signal with 50% or 90% efficiency, respectively $d^{50\%}$ and $d^{90\%}$. These values have been extracted from the results of the fits of the detection efficiency as a function of the distances for which the BBH sources have been simulated. An asymmetric sigmoid function has been used and the errors on $d^{50\%}$ and $d^{90\%}$ have been estimated as they have for $h_{rss}^{50\%}$ and $h_{rss}^{90\%}$. Figure 13 shows the $d^{50\%}$ and $d^{90\%}$ detection distances as a function of the total mass of the system. $d^{90\%}$ gives an indication of the average distance range up to which this search could have been able to detect a BBH source. With the present choice of threshold on

the SNR, our search is sensitive to BBH mergers in the mass range 20 $M_{\odot}$–150 $M_{\odot}$ up to a distance of 1–3 Mpc (0.5–1 Mpc) for 50% (90%) detection efficiency. The distance reach is maximum for a BBH of total mass 80–90 $M_{\odot}$. In the C7 sensitivity band, this mass range corresponds to signals where the merger part is dominant. Besides, for a mass higher than 100 $M_{\odot}$, the merger frequency (given by equation (12)) is below the frequency lower bound studied in the analysis (150 Hz). This fact adds to the degraded C7 run sensitivity below 150 Hz, and explains why the distance reach for the high mass waveforms is decreasing.

This bound on the distance can, in principle, be translated into an upper limit on the event rate, assuming a Gaussian distribution of BBH masses around 80 $M_{\odot}$. This analysis would require combining a model for the galaxies, their blue light luminosity distribution as a function of distance and mass, along with the antenna pattern of the detector; this has been proposed in [68] for the LIGO detectors. But given the limited volume of the universe that the present search is capable of sampling, we postpone this more complete analysis until we analyze the most recent Virgo data with its improved sensitivity. Moreover, the results have been obtained only for non-spinning equal mass binary systems.

An alternative way of deriving the distance reach for BBH mergers is to assume that the merger and ring-down phases of the BBH waveforms resemble Sine Gaussians and use the results obtained from the Sine Gaussian waveforms to derive the detection distance. In order to use Sine Gaussians to model the BBH mergers, we approximate the NR waveforms to be Sine Gaussians with peak frequency f_0 equal to the frequency at the merger (f_{merger}) of the NR waveforms using equation (12) following [25]. It should be noted that this definition of f_{merger} is only approximate. Besides, it is not obvious how to assign a precise value of Q to the Sine Gaussian that approximates a BBH waveform. However, taking into account the typical duration τ of the 'merger' part of the waveform and using the relation, exact for a Sine Gaussian, $\tau = Q/(2\pi f_0)$, one could deduce that the Q is between 10 and 20 for the high mass BBH and as large as 40 for the low masses. This is larger than the boundary of Sine Gaussian templates bank used in this analysis. Hence, we may suspect that for the low mass ($<$20 $M_{\odot}$) the EGC pipeline is not optimally reconstructing the SNR of the NR waveforms. However, it is straightforward to show that $h_{rss}^{50\%}$, the quantity which is used in the derivation, does not depend on Q for Sine Gaussians as long as Q is sufficiently large (table 3 confirms this). For all these reasons, in the discussion that follows, we consider a Sine Gaussian with $Q \sim 9$. In order to determine the distance reach one should make an assumption on the total energy emitted by the source and on the source emission pattern. According to NR simulations [63], $\sim$3.5% of the total rest mass energy would be radiated away as GWs. Following [25], we can use equation (14) and the values of h_{rss} in table 3 to derive the distances up to which such BBH merger events could be observed with an efficiency of 50% or 90%. The results for the distance reach at an efficiency of 90% are presented in figure 13 together with the distance reach obtained using NR waveforms at the same detection efficiency. At intermediate masses and frequencies the distance reach obtained when BBH mergers are modeled with SG waveforms is about 60% larger than that obtained when more realistic NR waveforms are used. A detailed comparison of the two waveforms shows that this difference is partly due to the broader spectral distribution of the NR waveform for which part of the signal energy falls out of the detector and analysis bandwidth. The remaining difference is due to the EGC pipeline, which by construction matches more efficiently with the SG waveforms.

7. Conclusion

In this paper, we have reported on a search for short duration GW bursts in the Virgo C7 data from within the 150 Hz–2 kHz frequency band; this corresponds to the best sensitivity

achieved by Virgo during the C7 run. This search, carried out using the output of only one GW detector, required first the understanding and then the possibility of vetoing all identified sources of noise. Special care has been taken to assure ourselves that the procedure does not suppress a GW event, and that the dead time remains small. Unfortunately, the non-stationary data features prevent a search during vetoed time periods, which amounts to an accumulated dead time of 20.2%. Though this rather large dead time limits the astrophysical interest of the search, it has been possible to calculate a sensitivity for various GW burst sources. The best sensitivity that has been reached in terms of the square root of the strain amplitude at 50% of efficiency, $h_{rss}^{50\%}$, was 1.1×10^{-20} Hz$^{-1/2}$ at 361 Hz, a frequency region where Virgo's sensitivity was optimal. If one considers the whole set of waveforms studied in this paper, the sensitivity lies between 10^{-20} and 10^{-19} Hz$^{-1/2}$. However, one should note that the error on the sensitivity can be as large as 40% due to uncertainties in the calibration of the strain amplitude. Those numbers can be compared to GW burst searches carried out with LIGO detectors during the S2 data taken in 2003 [22]. Indeed, the C7 Virgo sensitivity is comparable to that of 4 km LIGO detectors during their S2 run; Virgo during C7 was a little bit more sensitive above 500 Hz and a bit less below. Not surprisingly, the search sensitivity obtained with C7 Virgo data is similar to LIGO S2 results for the same kind of waveforms: $h_{rss}^{50\%}$ having values between 10^{-20} and 10^{-19} Hz$^{-1/2}$.

Besides the search of unmodeled GW burst waveforms, we have shown using recently computed numerical relativity waveforms that burst pipelines can be used efficiently to search for BBH merger GW emission. In the case of non-spinning equal mass system, a distance reach of 2.9 Mpc for 80 $M_{\odot}$ total mass has been inferred from the C7 data assuming an efficiency of 50%. This mass range corresponds to when the BH merger part of the signal dominates over the inspiral part. That also corresponds to a frequency region where ground base interferometers achieve their best sensitivity. It is interesting to note that the sensitivity in the merger dominated frequency range is up by roughly a factor of 10 in the most recent Virgo data (acquired in the later half of 2007). This would correspond to a distance reach up to 30 Mpc (12 Mpc) at 50% (90%) efficiency. This distance reach improvement is not enough to tackle regions where the number of galaxies becomes interesting given the expected BBH event rate. Further upgrades, like Advanced Virgo, may be needed to have a reasonable probability of detection. Despite that, and given the improvement of the Virgo sensitivity in the low frequency region, we will expand the EGC pipeline parameter space to explore more efficiently from this region. Though matched filtering with a bank of templates, including inspiral, merger and ring-down phases, might have a better detection efficiency for BBH mergers, it is important to complement the search with other techniques not based on tailored matched filtering but using generic templates, such as Sine Gaussians. This approach could provide a method that would be more robust at finding increasingly complicated signals that depend on a larger number of astrophysical parameters from the sources, such as a black hole's spin in the case of a black hole–neutron star system.

Finally, one should add that the recent Virgo data taking (VSR1) will be analyzed in coincidence with LIGO S5 data. That is especially interesting in the high frequency region (>600 Hz) where the sensitivity of the four detectors are all limited by shot noise. This network of four non-aligned interferometers with comparable sensitivity should be able to detect the GW signal emitted by a supernova anywhere in the galaxy.

Acknowledgments

The authors thank H Dimmelmeier for fruitful discussions and providing the new core collapse waveforms. We thank the numerical relativity group at NASA Goddard Space Flight Center

for sharing the results of their binary black hole simulations with us. We also want to thank B Kelly for valuable discussions about these waveforms.

References

[1] Acernese F *et al* (Virgo Collaboration) 2007 *Class. Quantum Grav.* **24** S381
[2] Acernese F *et al* (Virgo Collaboration) 2007 *Class. Quantum Grav.* **24** 5767
[3] Acernese F *et al* (Virgo Collaboration) 2007 *Class. Quantum Grav.* **24** S491
[4] Acernese F *et al* (Virgo, ROG and AURIGA Collaborations) 2008 *Class. Quantum Grav.* **25** 205007
[5] Acernese F *et al* (Virgo Collaboration) 2008 *Class. Quantum Grav.* **25** 225001
[6] Zwerger T and Mueller E 1997 *Astron. Astrophys.* **320** 209
[7] Dimmelmeier H, Font J A and Mueller E 2002 *Astron. Astrophys.* **393** 523
[8] Ott C D *et al* 2004 *Astrophys. J.* **600** 834
[9] Shibata M and Sekiguchi Y I 2004 *Phys. Rev.* D **69** 084024
[10] Ott C D *et al* 2006 *Phys. Rev. Lett.* **96** 201102
[11] Ott C D 2009 *Class. Quantum Grav.* **26** 063001
[12] Flanagan E E and Hughes S A 1998 *Phys. Rev.* D **57** 4535
[13] Baker J G *et al* 2006 *Phys. Rev.* D **73** 104002
[14] Pretorius F 2005 *Phys. Rev. Lett.* **95** 121101
[15] Campanelli M *et al* 2006 *Phys. Rev. Lett.* **96** 111101
[16] Kokkotas K D and Schmidt B G 1999 Quasi-normal modes of stars and black holes *Living Rev. Rel.* **2** 12–22 http://www.livingreviews.org/lrr-1999-2
[17] Meszaros P 2006 *Rep. Prog. Phys.* **69** 2259–322
[18] Ferrari V, Miniutti G and Pons J A 2003 *Class. Quantum Grav.* **20** S841
[19] Damour T and Vilenkin A 2005 *Phys. Rev.* D **71** 063510
[20] Postnov K A and Yungelson L R 2006 The evolution of compact binary star systems *Living Rev. Rel.* **6** 36–8 http://www.livingreviews.org/lrr-2006-6
[21] O'Shaughnessy R, Kim C, Frakgos T, Kalogera V and Belczynski K 2005 *Astrophys. J.* **633** 1076
[22] Abbott B *et al* (LSC) 2005 *Phys. Rev.* D **72** 062001
[23] Pretorius F 2007 *Relativistic Objects in Compact Binaries: From Birth to Coalescence* ed Colpi (Berlin: Springer) arXiv:0710.1338
[24] Abbott B *et al* (LSC) 2004 *Phys. Rev.* D **69** 102001
[25] Abbott B *et al* (LSC) 2007 *Class. Quantum Grav.* **24** 5343–69
[26] Astone P *et al* 2003 *Phys. Rev.* D **68** 022001
[27] Ando M *et al* (TAMA Collaboration) 2005 *Phys. Rev.* D **71** 082002
[28] Baker J G *et al* 2007 *Phys. Rev.* D **75** 123024
[29] Acernese F *et al* (Virgo Collaboration) The Virgo detector *NIM* unpublished
[30] Braccini S *et al* (Virgo Collaboration) 2005 *Astropart. Phys.* **23** 557
[31] Acernese F *et al* (Virgo Collaboration) 2008 *Astropart. Phys.* **30** 29–38
[32] Rolland L 2008 Private communication
[33] Anderson W G *et al* 2001 *Phys. Rev.* D **63** 042003
[34] Klimenko S and Mitselmakher G 2004 *Class. Quantum Grav.* **21** S1819
[35] Guidi G M *et al* 2004 *Class. Quantum Grav.* **21** S815
[36] Chatterji S *et al* 2004 *Class. Quantum Grav.* **21** S1809
[37] Clapson A-C *et al* 2008 *Class. Quantum Grav.* **25** 035002
[38] Arnaud N *et al* 2003 *Phys. Rev.* D **67** 102003
[39] Hoshen J and Kokelman R 1976 *Phys. Rev.* B **14** 3438
[40] Beauville F *et al* 2008 *Class. Quantum Grav.* **25** 045002
[41] Arnaud N *et al* 2003 *Phys. Rev.* D **67** 062004
[42] Acernese F *et al* (Virgo Collaboration) 2004 *Class. Quantum Grav.* **21** S425
[43] Flaminio R, Gouaty R and Tournefier E Virgo technical document, VIR-NOT-LAP-1390-313
[44] Christensen N, Shawhan P and González G (for the LIGO Scientific Collaboration) 2004 *Class. Quantum Grav.* **21** S1747
[45] Koetter K, Heng I, Hewitson M, Strain K, Woan G and Ward H 2003 *Class. Quantum Grav.* **20** S895–902
[46] Hanna C R (for the LSC Collaboration) 2006 *Class. Quantum Grav.* **23** S17–22
[47] Christensen N (for the LSC Collaboration) 2005 *Class. Quantum Grav.* **22** S1059–68
[48] Caron B *et al* 1999 *Astropart. Phys.* **10** 369

[49] Baker J G *et al* 2006 *Phys. Rev.* D **73** 104002
[50] http://www.mpa-garching.mpg.de/rel_hydro/
[51] Christensen N 1992 *Phys. Rev.* D **46** 5250
[52] Dimmelmeier H *et al* 2007 *Phys. Rev. Lett.* **98** 251101
[53] Dimmelmeier H *et al* 2008 *Phys. Rev.* D **78** 064056
[54] Ott C D *et al* 2007 *Phys. Rev. Lett.* **98** 261101
[55] Bruegmann B *et al* 2004 *Phys. Rev. Lett.* **92** 211101
[56] Buonanno A, Cook G B and Pretorius F 2007 *Phys. Rev.* D **75** 124018
[57] Baker J G *et al* 2007 *Phys. Rev. Lett.* **99** 181101
[58] Berti E *et al* 2007 *Phys. Rev.* D **76** 064034
[59] Hannam M *et al* 2008 *Phys. Rev.* D **77** 044020
[60] Baker J G *et al* 2007 *Class. Quantum Grav.* **24** S25–31
[61] Ajith P *et al* 2007 *Class. Quantum Grav.* **24** S689–700
[62] Pan Y *et al* 2008 *Phys. Rev.* D **77** 024014
[63] Baker J G *et al* 2006 *Phys. Rev.* D **73** 104002
[64] Brady P R, Creighton J D E and Wiseman A G 2004 *Class. Quantum Grav.* **21** S1775
[65] Shapiro S L and Teukolsky S A 1983 *BlackHoles, White Dwarfs and Neutron Stars* (New York: Wiley)
[66] Riles K LIGO technical document, LIGO-T040055-00-Z
[67] Shen H *et al* 1998 *Prog. Theor. Phys.* **100** 1013
[68] Kopparapu R K *et al* 2008 *Astrophys. J.* **675** 1459